






## Symmetry breaking in magnetoresistive devices

Ricci Erlandsen <sup>1</sup>, Rasmus Bjørk <sup>1</sup>, Lior Kornblum <sup>2</sup>, Nini Pryds <sup>1</sup> and Dennis V. Christensen <sup>1,\*</sup>

<sup>1</sup>*Department of Energy Conversion and Storage, Technical University of Denmark, DK-2800 Kgs. Lyngby, Denmark*

<sup>2</sup>*Andrew and Erna Viterbi Department of Electrical & Computer Engineering, Technion–Israel Institute of Technology, Haifa 32000-03, Israel*



(Received 7 December 2020; revised 17 December 2021; accepted 31 May 2022; published 12 July 2022)

Detecting weak magnetic fields is paramount in areas such as scanning magnetometers and manipulation of magnetic nanoparticles, thus rendering it crucial to increase the weak-field sensitivity for developing next-generation magnetic sensors. The current approaches for high-sensitivity sensors, such as superconducting quantum interference devices, are complex and expensive. By contrast, magnetoresistive sensors and particularly extraordinary magnetoresistive sensors offer a simple operation at room temperature but, to date, at inferior sensitivity. To overcome these challenges, we induce device symmetry breaking to enhance the weak magnetic field sensitivity in semiconductor-metal hybrid structures exhibiting extraordinary magnetoresistance. Retaining the device mirror symmetry yields symmetric magnetoresistance curves with  $R(B) = R(-B)$ , which results in inferior detection of weak magnetic fields as  $[dR/dB]_{B \rightarrow 0} = 0$ . Using finite element modeling, we study the change in device behavior as the symmetry is broken by varying the device geometry by spatially varying the constituent material properties or both. We show that symmetry breaking has three important implications: First, breaking the mirror symmetry causes an asymmetric sensor response with  $R(B) \neq R(-B)$ , benefiting from a largely enhanced sensitivity to weak magnetic fields and detection of the magnetic field direction. Second, an interplay with the Hall effect causes a large negative magnetoresistance exceeding 79% at  $B = 1$  T and room temperature without magnetic constituents or explicit optimization of this property. Third, the asymmetric geometries can be used as a key ingredient toward designing on-demand magnetoresistive characteristics such as linearity at low magnetic fields, step functions, and magnetic switchlike behavior. These implications pave the way for asymmetric topology optimization of magnetoresistive devices with unparalleled performance.

DOI: [10.1103/PhysRevB.106.014408](https://doi.org/10.1103/PhysRevB.106.014408)

### I. INTRODUCTION

Detection of magnetic fields with magnetoresistive sensors has been the cornerstone in essential components for decades, with applications ranging from magnetic hard disks [1,2] to detection and manipulation of magnetic nanoparticles in biomagnetic fields [3–6]. Magnetoresistive sensors based on, e.g., giant magnetoresistance (GMR) devices are simple, technologically mature, operational at room temperature, and compatible with mass production [7–11]. Despite extensive research, the sensors generally still lack the sensitivity required for detecting ultraweak magnetic fields (femtotesla to picotesla) often associated with signals detected in the human body [12].

The extraordinary magnetoresistance (EMR) was discovered in semiconductor-metal hybrid structures in 2000 by Solin *et al.* [13] with reported magnetoresistance values exceeding 10<sup>6</sup>% at room temperature in an applied magnetic field of 5 T [13,14]. The EMR is governed by the Lorentz force, which causes a current redistribution when a magnetic field is applied [15,16]. A semiconductor-metal EMR device resembles a short circuit at zero magnetic field with a significant part of the current flowing through a metal inclusion. At increasing magnetic fields, highly resistive states

are obtained as the current is deflected around the metal inclusion. The EMR features room-temperature operation with no magnetic components causing magnetic noise and stray fields that can alter the test subjects. The effect is purely geometrical, however, some material parameters of the hybrid structures are crucial, such as a high electron mobility of the semiconductor and a high electrical conductivity of the metal [17,18]. Therefore, intense research has been conducted using various high-mobility materials, including InSb [13,17–22], GaAs [23–26], and graphene [27–31]. Optimizing the device geometry was further found to highly increase device performance where shaping the metallic inclusion as a symmetric Hall bar [14,32] or square [33] was shown to enhance the MR response by several orders of magnitude. However, to date, geometric optimization was done only on symmetric structures [2,14,32–40]. These symmetric EMR devices produce large MR values with a symmetric magnetoresistance response where  $R(B) = R(-B)$  around zero magnetic field [13,15,19,32,33,41]. The symmetric behavior leads to the sensitivity  $[dR/dB]_{B \rightarrow 0} = 0$ , which is undesirable for detecting weak magnetic fields [40,42]. Asymmetric geometries in EMR devices can therefore provide a way to tune the device, beyond previous studies on inducing asymmetry in the magnetoresistance of EMR devices by changing the contact configuration [2,33,34,36,38,40,42–45]. This forms an alternative approach where the asymmetries are directly built into the EMR device itself to form an asymmetric sensor response,

\*dechr@dtu.dk

independently of the contact location. The entire shape of the EMR device thus can be used to induce asymmetries, providing ample room for optimization of the EMR performance. This may constitute an important step toward resolving the challenge of detecting weak magnetic fields using magnetoresistive devices.

Here, we start with the archetypal EMR device of two concentric discs where the larger outer circle consists of semiconducting InSb and with the smaller inner disk of metallic Au [13]. We study the effects of inducing asymmetries in the device to obtain an understanding of the origin of negative and asymmetric magnetoresistance in EMR devices and to examine how asymmetry can be harnessed into a tuning knob for the development of future sensors capable of detecting weak magnetic fields.

## II. METHODS

In this paper, we consider the hybrid structure schematized in Fig. 1(a), with the current ( $I$ ) being injected between the lower pair of contacts as depicted by the arrows. The results shown are independent of the current, which for convenience is chosen to be 1 A in absence of Joule heating. The difference in electric potential ( $\Delta V$ ) is deduced between the upper pair of contacts. The four-terminal resistance,  $R = \Delta V/I$ , is used to extract the magnetoresistance (MR) as a function of magnetic field applied perpendicular to the device ( $B$ ):

$$\text{MR} = \frac{R(B) - R(0)}{R(0)}. \quad (1)$$

Due to the planar structure of EMR devices, we utilize a 2D finite element model via COMSOL MULTIPHYSICS version 5.5. The current flow is governed by Ohm's law,  $\mathbf{j} = \sigma \mathbf{E}$ , where  $\mathbf{j}$  is the current density vector,  $\sigma$  is the conductivity tensor, and  $\mathbf{E}$  is the electrical field. The 2D conductivity tensor depends both on the magnetic field and material parameters by

$$\sigma(B) = \frac{\sigma_0}{1 + (\mu B)^2} \begin{bmatrix} 1 & -\mu B \\ \mu B & 1 \end{bmatrix}, \quad (2)$$

where  $\mu$  is the electron mobility of the semiconductor and  $B$  is the perpendicular magnetic field. The Drude conductivity at zero magnetic field is given as  $\sigma_0 = ne\mu$ , where  $n$  is the carrier density. The model solves the continuity equation of the electrostatic potential  $\phi(x, y)$  under steady-state conditions:

$$\nabla \cdot [\sigma \nabla \phi(x, y)] = 0. \quad (3)$$

The device and materials are based on the work by Solin *et al.* [13], which utilizes InSb ( $\sigma = 1.86 \times 10^4 \Omega^{-1}\text{m}^{-1}$ ,  $\mu = 45\,500 \text{ cm}^2/\text{Vs}$  at RT) as the semiconductor and gold ( $\sigma_0 = 4.52 \times 10^7 \Omega^{-1}\text{m}^{-1}$ ,  $\mu_0 = 50 \text{ cm}^2/\text{Vs}$  at room temperature) as the metal. The thickness of InSb,  $t = 1.3 \mu\text{m}$ , was used to calculate the resistance with  $R \propto 1/t$ . The gold contacts to the semiconductor are modeled as four boundaries on the perimeter of the semiconductor disk with angular widths of  $9^\circ$ . The Laplace equation [Eq. (3)] is solved under the boundary condition that no current flows at the perimeter of the semiconductor disk, except where the source and drain contacts are placed.

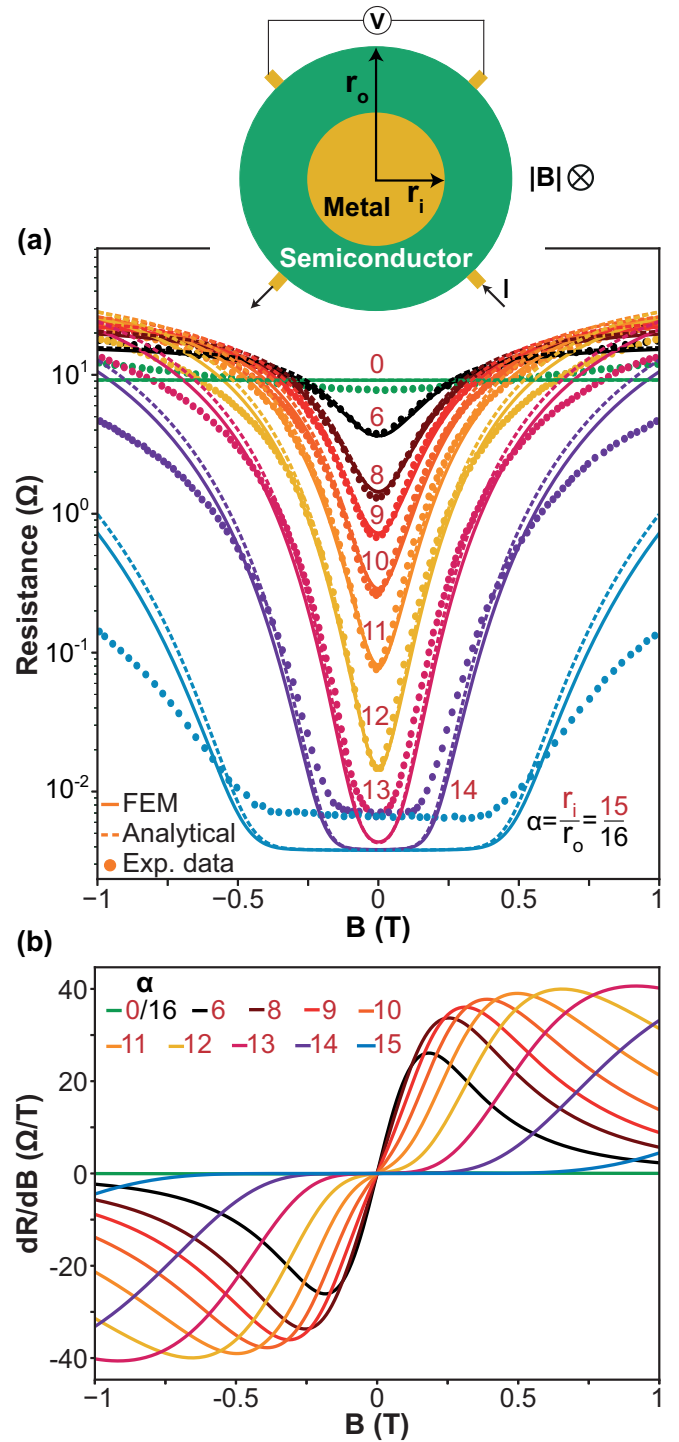


FIG. 1. Resistance versus magnetic field ( $B$ ) at varying filling factors,  $\alpha = r_i/r_o$ , where  $r_i$  and  $r_o$  denote the radii of the metal and semiconductor part, respectively, as shown in the device schematic (top). (a) Plot showing finite element modeling (FEM) simulations (solid lines), analytical solution [46] (dashed lines) and experimental data [13] (dots). (b) Sensitivity as a function of magnetic field for the same filling factors used in (a)

The geometrical ratio between semiconductor and metal disk sizes is defined as the filling factor,  $\alpha = r_i/r_o$ , where  $r_i$  and  $r_o$  are the radii of the inner and outer semiconductor disks, respectively. The device performance is independent

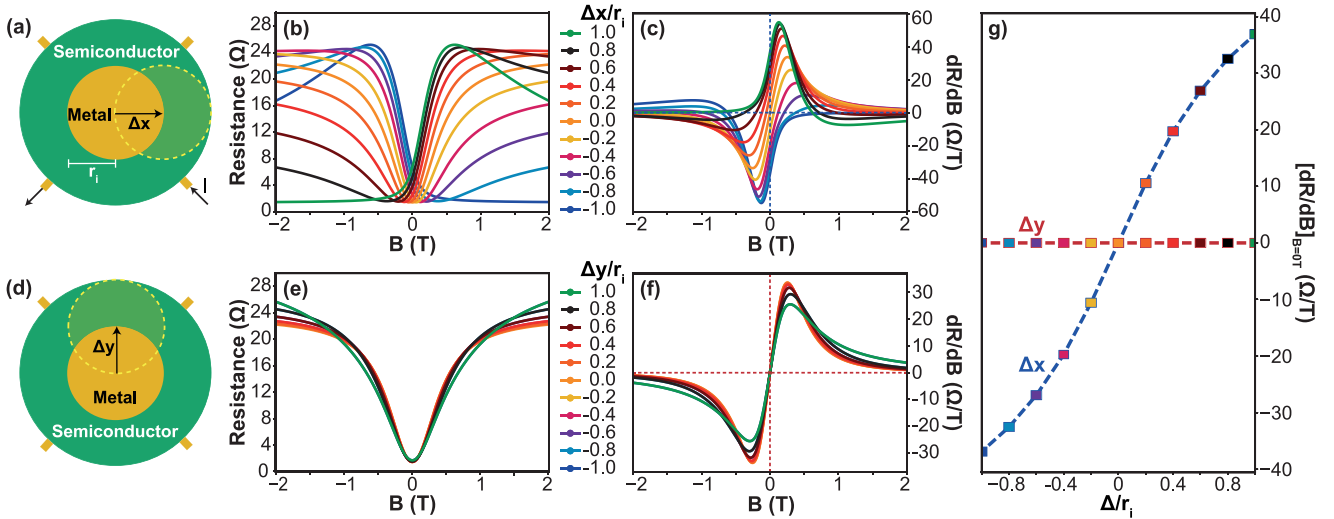


FIG. 2. Effects of displacing the metal inclusion in EMR devices. (a) Device schematic showing displacement of the metal in the horizontal direction denoted as  $\Delta x$ . The radius of the metallic circle is denoted by  $r_i$ . (b) Resistance as a function of magnetic field for varying  $\Delta x$ , as depicted by values of  $\Delta x/r_i$ . (c) Sensitivity versus magnetic field for varying  $\Delta x$ , showing that breaking the mirror symmetry affects device performance. (d) Device schematic showing displacement along the vertical direction ( $\Delta y$ ). (e) Resistance as a function of magnetic field for varying vertical displacements given in units of  $\Delta y/r_i$ . (f) Sensitivity versus magnetic field for varying  $\Delta y$ , showing that retaining mirror symmetry has a negligible effect on the device. (g) Sensitivity evaluated at zero field as a function of displacement for  $\Delta x$  (blue) and  $\Delta y$  (red), matching the dashed lines in (c) and (f), respectively. The dashed lines are a guide for the eye.

of the total size of the device and we arbitrarily set  $r_o = 1$  mm. The sensitivity,  $dR/dB$ , was calculated by numerical differentiation using the central difference principle with a magnetic field resolution of 10 mT. A stable mesh size was determined to be above 5000 grid elements (Supplemental Material, Fig. S1 [47]).

### III. SYMMETRIC EMR DEVICES

Calculating  $R(B)$  at varying filling factors allows us to directly compare our model to experimental data [13] along with an analytical solution [46] (Supplemental Material, Eq. (S1) [47]), as shown in Fig. 1(a). The sensitivity of the different filling factor values are shown in Fig. 1(b). Our FEM model is in excellent agreement with the analytical solution available for this high-symmetric geometry as well as reproducing the major trends from experiments. The deviation from the experimental data for  $\alpha > \frac{12}{16}$ , has previously been attributed to the model, not accounting for contact resistance at the metal-semiconductor interface [15,46].

The MR is shown as a function of increasing filling factor  $\alpha$  in Supplemental Material, Fig. S2 [47]. For 0.05, 0.1, and 0.25 T, the largest MR values were achieved with  $\alpha = \frac{12}{16}$ , where 1 T revealed a maximum at  $\alpha = \frac{13}{16}$  with MR = 530 00%, displaying good reproducibility of previously published results [13–15]. Symmetric devices yield resistance curves that are symmetric around zero magnetic field, causing the sensitivity to approach zero as  $B \rightarrow 0$  T as shown in shown in Fig. 1(b). To detect weak magnetic fields with symmetric devices, a bias magnetic field must be applied to move this device into the most sensitive region. For the material properties and device geometry used here, the maximum sensitivity reaches around 40  $\Omega/T$  at large fields of around 0.5 T. The need for applying a bias fields both complicates

sensor architecture and may cause influence on the test subjects. Thus, measuring weak magnetic field requires a strategy which breaks the symmetry of the MR curves.

### IV. BREAKING THE SYMMETRY

In the following, we have studied the effect of breaking the geometrical symmetry by displacing the metal disk along the vertical and horizontal axes as illustrated in Figs. 2(a) and 2(d). We denote displacement along the horizontal axis as  $\Delta x$ . For illustrative purposes, we chose the ratio of  $\alpha = \frac{8}{16}$ , as this provided a larger range in which the metal disk can be displaced, although this provides a smaller MR compared to  $\alpha = \frac{13}{16}$ . The metal disk was displaced in steps of 0.1 mm up to a maximum  $\Delta x$  of 0.5 mm.

Figure 2(b) shows  $R(B)$  at varying displacements along  $\Delta x$ , given in units of the metal disk radius,  $\Delta x/r_i$ . The device is considerably affected by the symmetry breaking with an equal displacement of the metal disk in opposite directions yielding mirror-symmetric curves with  $R(B, \Delta x) = R(-B, -\Delta x)$ , as also phenomenologically illustrated in Supplemental Material, Fig. S3 [47]. The resistance increases and the sensitivity at  $B = 0$  T becomes nonzero with larger displacements. An interesting feature of the  $\Delta x$  displacement is not only the appearance of a maximum in the resistance at about  $B = 0.5$  T for  $\Delta x/r_i = 1$  but also the negative slope for negative magnetic fields. The sensitivity for varying  $\Delta x$  is shown in Fig. 2(c) with a peak at 0.13 T, where the sensitivity increases as the system becomes more displaced, yielding a maximum  $dR/dB = 54$   $\Omega/T$ . Not only does the sensitivity increase but it also becomes nonzero for  $B \rightarrow 0$ . We have repeated the procedure of displacing the metal disk, but in the vertical direction,  $\Delta y$ , illustrated in Fig. 2(d). The changes of  $R(B)$  at varying vertical displacements are shown in Fig. 2(e).

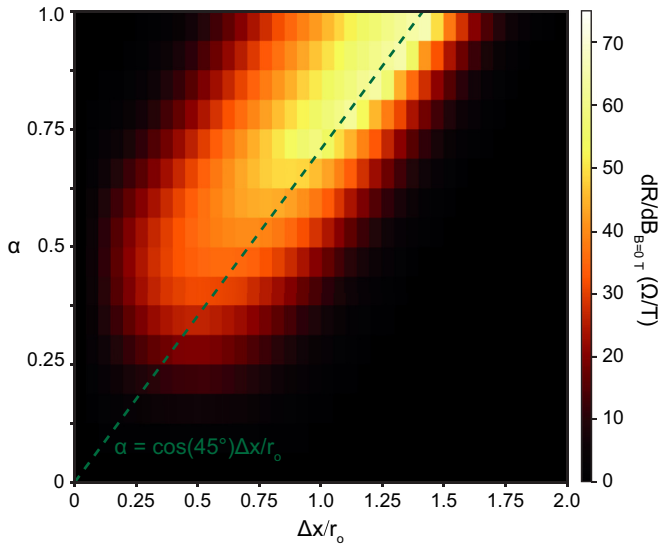


FIG. 3. Zero-field sensitivity as a function of filling factor  $\alpha$  and the normalized displacement of the metal disk,  $\Delta x/r_o$ . The green dashed line represents the function  $\alpha_{\text{opt}} = \cos(45^\circ)\Delta x/r_o$  (see main text)

We observed no large effect of shifting the center of the metal disk by any value of  $\Delta y$ . Changing the metal placement in the  $y$  direction will have an impact on  $\sigma_0$ , but as shown in Fig. 2(f), the sensitivity barely changes and is similar to the case of  $\alpha = \frac{8}{16}$  in Fig. 1(b). The symmetry of the mirroring axis between the pair of voltage probes is retained, which renders the MR curves symmetric and  $dR/dB = 0$  under  $\Delta y$  displacements (see Supplemental Material, Fig. S3 [47]).

The sensitivity at weak magnetic fields is especially interesting for some applications, such as detecting biomagnetism [3–6,12]. As shown, displacing the metal inclusion can enhance  $dR/dB$  at weak fields through an interplay between the Lorentz force and the asymmetric geometry. We calculate  $dR/dB$  for  $B \rightarrow 0$  for both  $\Delta x$  and  $\Delta y$ , as shown in Fig. 2(g). As expected, the sensitivity under  $\Delta y$  displacement was constant throughout the whole range with a value of zero, whereas the sensitivity increased monotonically with  $\Delta x$  displacements up to  $37 \text{ } \Omega/\text{T}$  for  $\Delta x/r_i = 1$ . Thus, we shift the maximum sensitivity previously found at large fields of around  $0.5 \text{ T}$  [Fig. 1(b)] to  $0 \text{ T}$ , eliminating the need for a bias field to measure small magnetic field strengths. We further vary both the displacement along the  $x$  axis for different radii of the metal disk. As displayed in Fig. 3, the sensitivity is a nonmonotonic function of both parameters where the optimal metal radius varies with the displacement. Interestingly, for  $\alpha = 8/16$  the optimal value of the displacement is  $\Delta x_{\text{opt}}/r_o = 0.7 = \cos(45^\circ)$ , which corresponds to the situation where the metal disk is offset such that its center is directly between the current and voltage probe. Here, the metal disk protrudes outside the semiconductor, in contrast to Fig. 2 where the metal disk was restricted to be inside the semiconductor disk. The optimum for  $\alpha = 8/16$  is placed on a roughly linear relationship between the optimal filling factor as a function of displacement ( $\alpha_{\text{opt}} = \cos(45^\circ)\Delta x/r_o$ ) as indicated with the green dashed line in Fig. 3. To a first

approximation, the relationship approximately describes the conditions where the metal is shorting the right current and voltage probe for  $\Delta x/r_o > 1$ , suggesting that the number of contacts may be decreased without loss of sensitivity. Within this simple optimization scheme, the sensitivity increases by a factor of  $\simeq 2$  from  $37 \text{ } \Omega/\text{T}$  at  $\Delta x \cdot r_o = 0.5$  and  $\alpha = 8/16$  to  $66 \text{ } \Omega/\text{T}$  at  $\Delta x \cdot r_o = 1.4$  and  $\alpha = 15/16$ . This increase in the zero-field sensitivity is beyond what is achievable with the highly symmetric case at any magnetic field [Fig. 1(b)], signifying that it is possible both to shift the optimal magnetic field range to  $0 \text{ T}$  as well as to improve the best sensitivity. This also indicates the opportunity for further optimization using a more comprehensive geometrical optimization scheme and in particular changing the location and number of contacts. The electron mobility of the semiconductor is a crucial factor in EMR devices [14,15,36,48]. Figures 4(a)–4(c) show how the mobility affects both symmetric and asymmetric ( $\Delta x/r_i = 1$ ) devices. Figure 4(a) shows  $R(B)$  of a symmetric device for various electron mobilities. A lower electron mobility will decrease the conductivity at zero field, while high mobility will not only increase  $\sigma_0$  but also lead to sharper MR responses and faster saturation when applying the magnetic field. The asymmetric case in Fig. 4(b) shows the same tendencies, with a small step in resistance from  $B = 0$  to around  $0.2 \text{ T}$  at high mobilities, where a low mobility will increase the overall resistance of the system and smear out the step. Figure 4(c) depicts the MR as a function of the mutual scaling factor,  $\mu B$ . In both cases, the MR curves for varying mobilities follow the same scaling forming a single collapsed curve. This follows from the conductivity tensor [Eq. (2)] where the Lorentz force governing the EMR is a function of  $\mu B$ . In essence, this entails that a large MR response can be achieved by either having a high mobility or increasing the magnetic field. In cases where a high magnetoresistive response is desired for weak magnetic fields, it is therefore crucial to have a high electron mobility. Moreover, the scaling implies that from a single experiment or simulation where the MR is measured (simulated) as a function of the magnetic field, one can deduce the effect of changing the electron mobility. This applies to both the symmetric and asymmetric cases.

Another approach to break the device symmetry is by splitting the semiconducting disk into two regions named S1 and S2. By fixing the mobility of S1,  $\mu_{S1} = 45\,500 \text{ cm}^2/\text{Vs}$ , and varying only  $\mu_{S2}$ , it is possible to induce asymmetry in the system (see Fig. 3). This can, e.g., be obtained by intentional degradation of the mobility of a high mobility semiconductor on half of the semiconductor. A possible approach is to protect the high mobility side with a thick photoresist or a hard mask and then perform ion implantation (He, H, Ar, etc.) to form point defects that reduce the mobility. Design of the implantation parameters versus the ion type and semiconductor thickness can provide excellent control on the properties. Here, we additionally implement the displacement of the metal disk. Figures 4(d)–4(f) show  $R(B)$  for the two-material system with a centered metal disk (d),  $\Delta x/r_i = 1$  (e), and  $\Delta x/r_i = -1$  (f). We observe that the centered metal disk configuration has asymmetry, while the features when displacing the metal disk to the right is similar to the single-material system, yet more pronounced. Displacing the metal disk to the left or right has a similar steplike feature in the resistance

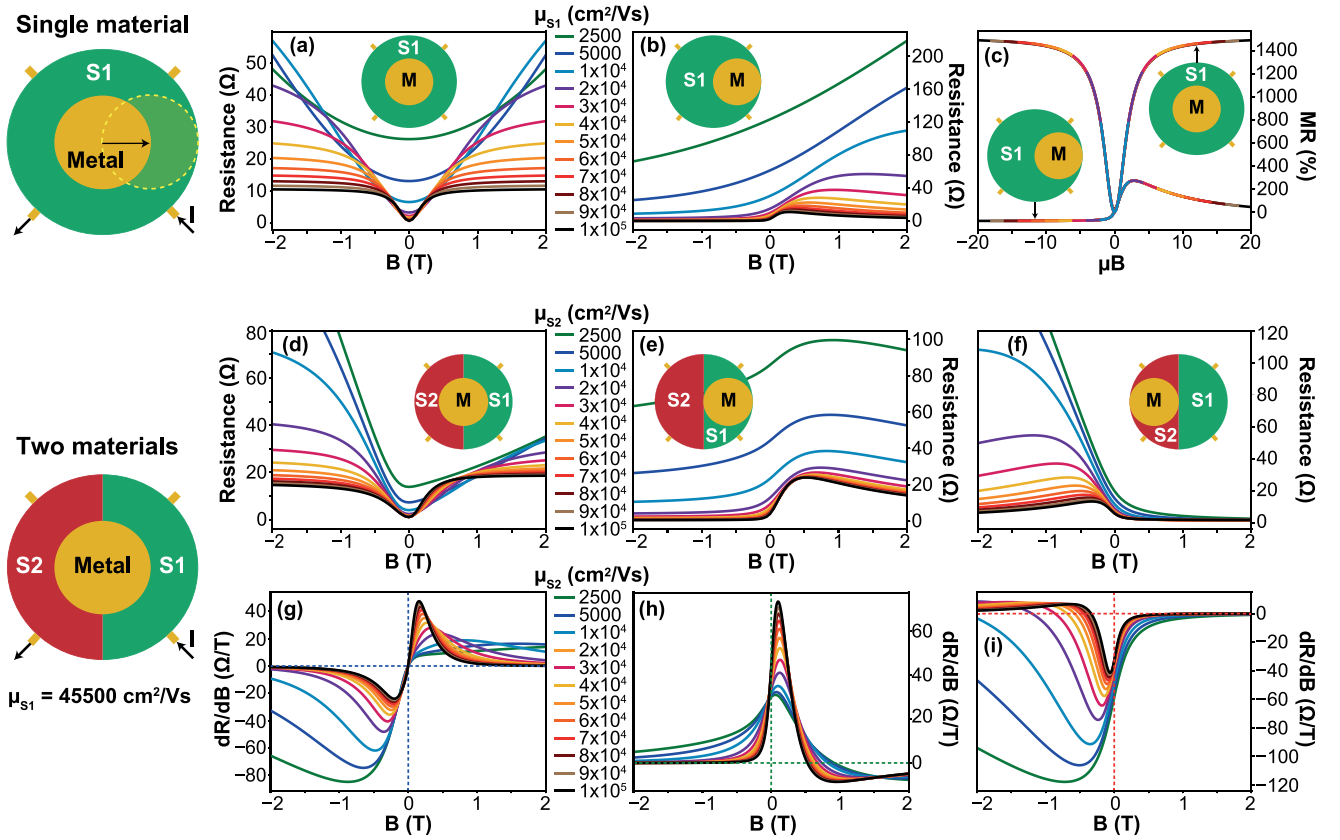


FIG. 4. Upper panels:  $R(B)$  for varying electron mobilities in the case of a single-material semiconducting disk with a symmetric device configuration (a) and asymmetric configuration where  $\Delta x/r_i = 1$  (b). MR values were extracted for both device configurations and plotted in (c) as a function of the mutual scaling factor,  $\mu B$ . Lower panels:  $R(B)$  and sensitivity plots illustrating the effects of utilizing two semiconducting materials (S1 and S2). The electron mobility of S1 was kept fixed at  $\mu_{S1} = 45\,500 \text{ cm}^2/\text{Vs}$  while varying  $\mu_{S2}$ . (d)–(f)  $R(B)$  for the two-material device with a centered disk of metal (d), displaced metal disk with  $\Delta x/r_i = 1$  (e), and  $\Delta x/r_i = -1$  (f). Sensitivity plots are shown in (g)–(i) corresponding to the configurations in (d)–(f), respectively, with the dashed lines representing zero field and zero sensitivity as a guide for the eye.

for high values of  $\mu_{S2}$ . As the mobility is decreased, the step-profile turns into a diodelike behavior with small resistance for  $B > 0$  and a rapidly increasing resistance for  $B < 0$  for the negatively offset device. In contrast to the single-material case, the simple  $\mu B$  scaling factor cannot be used to describe the two-material system (Supplemental Material, Fig. S4 [47]), as the current deflection in the semiconductor materials is spatially varying. However, even with an inaccurate mutual scaling factor, the two-material system produces a large MR response ( $> 1500\%$ ).

The sensitivity of the two-material device shown in Figs. 4(g)–4(i) is generally larger compared to the single-material device. The two-material device with a centered metal disk reaches a sensitivity of  $|dR/dB|_{B=1 \text{ T}} = 85 \text{ } \Omega/\text{T}$  for the lowest mobility  $\mu_{S2} = 2500 \text{ cm}^2/\text{Vs}$ . This device shows zero sensitivity for  $B \rightarrow 0$  [Fig. 4(g)], which is similar to the single-material case. Shifting the metal disk to the right yields a sharp sensitivity peak around 10 mT with a value of  $73 \text{ } \Omega/\text{T}$  for the highest mobility  $\mu_{S2} = 100\,000 \text{ cm}^2/\text{Vs}$  as shown in Fig. 4(h). This is comparable to the sensitivity of  $54 \text{ } \Omega/\text{T}$  from the fully displaced single material which saw a similar peak at roughly the same magnetic field strength. The highest sensitivity is found when shifting the metal disk left

into S2, which gives a value of  $|dR/dB|_{B=0.75 \text{ T}} = 120 \text{ } \Omega/\text{T}$  for  $\mu_{S2} = 2500 \text{ cm}^2/\text{Vs}$ . From this, we can conclude that shifting the metal disk right leads to better performance from a higher  $\mu_{S2}$ , where shifting it left benefits from a lower  $\mu_{S2}$ . For the majority of magnetic field values used here, the MR is considerably lower for the asymmetric device as seen in Fig. 4(c). However, Fig. 5(a) shows that the asymmetric device has a higher weak-field sensitivity, with a negligible dependence on electron mobility. This is interesting as it suggests that, in the single-material case, the mobility does not affect the sensitivity at zero magnetic field, however, only at finite magnetic fields. Contrarily, when using two materials to break the mirror symmetry, the varied mobility affects the zero-field sensitivity considerably and can both enhance or decrease it as shown in Fig. 5(b). The device with a metal disk in the S2 region of low mobility (left displacement) has a zero-field sensitivity that reaches a maximum  $|dR/dB|_{B \rightarrow 0} = 60 \text{ } \Omega/\text{T}$ , where the right-displaced system shows a maximum  $|dR/dB|_{B \rightarrow 0} = 40 \text{ } \Omega/\text{T}$  for the highest mobility. Asymmetric device geometry is a promising aspect of EMR devices and can be tailored to suit specific demands by varying the mobility in one region of the device. We have shown that by shifting the metal disk, it is possible to increase the

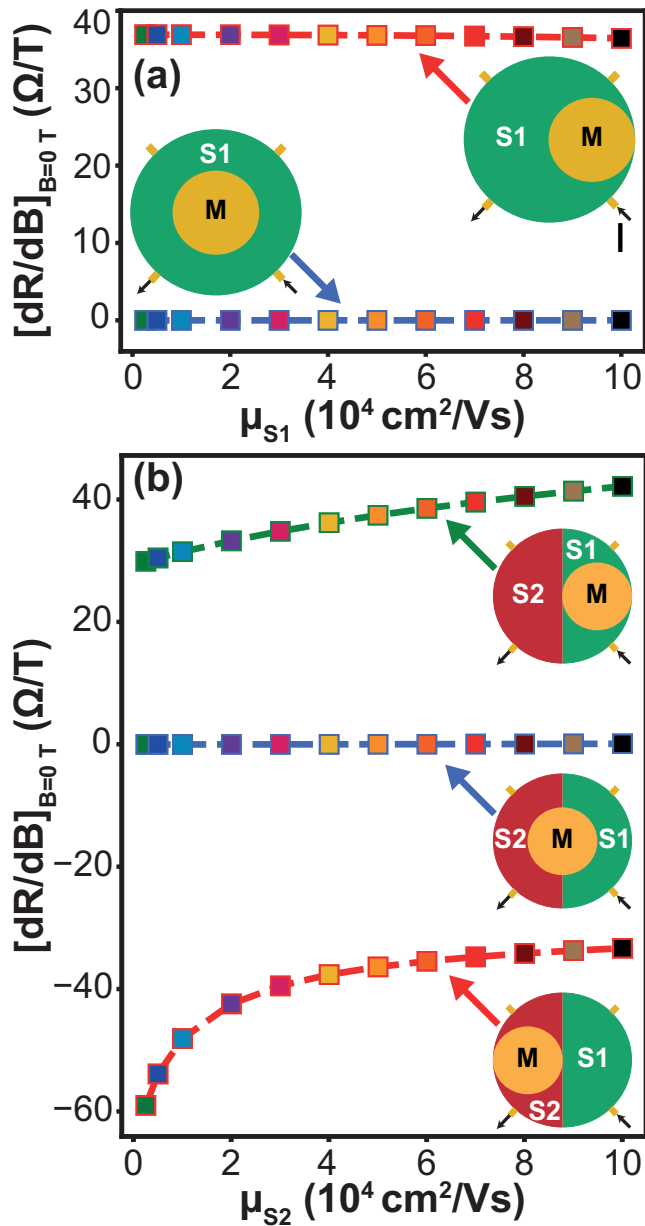


FIG. 5. Zero-field sensitivity as a function of  $\mu_{S2}$  with a fixed  $\mu_{S1} = 45500 \text{ cm}^2/\text{Vs}$ . (a) Single-material devices with symmetric (blue) and asymmetric (red) configuration. (b) Two-material devices with symmetric (blue), right-displaced (green), and left-displaced (red) configurations. The sensitivity values were extracted following the colored dashed lines in Figs. 4(g)–4(i).

weak-field sensitivity. Asymmetry can also be achieved by material junctions of varying electron mobilities which can potentially be sensitive to only one magnetic field direction as indicated in Fig. 4(f). The results also indicate that asymmetry can produce devices that have steplike sensor responses as seen in Fig. 4(e) or diode-like behavior as shown in Fig. 4(f). A study by Solin *et al.* [49] reports a sensitivity of  $147 \text{ }\Omega/\text{T}$  at  $B = 0.05 \text{ T}$  and a bias field of  $0.27 \text{ T}$ . A previous study where InAs was used as the active semiconducting material have reported a sensitivity of  $562 \text{ }\Omega/\text{T}$  at  $75 \text{ K}$  and  $0.26 \text{ T}$  [50] while another group reports  $67 \text{ }\Omega/\text{T}$  at RT and  $45 \text{ mT}$  which

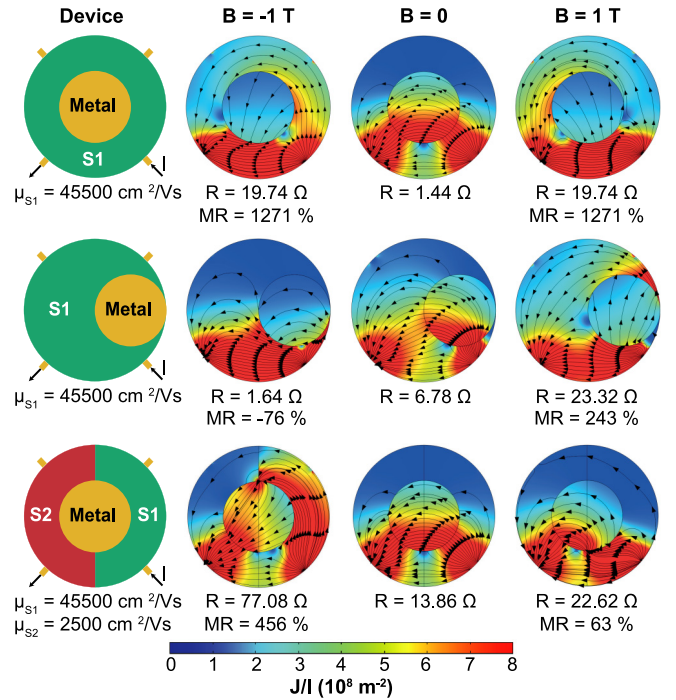


FIG. 6. Current flow affected by asymmetry and magnetic fields. Current injection is marked by the black arrows in the device schematics (left column). Current flow with magnetic fields of  $-1$ ,  $0$  and  $1 \text{ T}$  are depicted for the symmetric single-material device ( $\Delta x = \Delta y = 0$ , top row), fully displaced single-material system (middle row) and the two-material device ( $\mu_{S1} = 45500 \text{ cm}^2/\text{Vs}$  and  $\mu_{S2} = 2500 \text{ cm}^2/\text{Vs}$ ) with a centered metal disk (bottom row). Resistance and MR values are stated below each case. Color scale depicts  $J/I$  in units of  $10^8 \text{ m}^{-2}$ , where  $J$  is the local current density and  $I$  is the input current.

is similar to GMR sensors used in recording applications [45]. We report a sensitivity of  $60 \text{ }\Omega/\text{T}$  for  $B \rightarrow 0$  at RT. Considering our nonoptimal geometry with no bias field, our results provide valuable guidelines for designing future sensors with superior weak-field sensitivity.

## V. CURRENT FLOW IN EMR DEVICES

Understanding the current flow of the EMR device could help decipher the effects of displacing the metal inclusion. We have investigated the current flow at magnetic fields of  $-1$ ,  $0$ , and  $1 \text{ T}$  for the symmetric system, fully displaced single-material system, and the two-material system with a centered metal disk as shown in Fig. 6. With zero field and zero displacement, most of the current flows through the metal which results in  $R(0) = 1.44 \text{ }\Omega$ . The deflection from either a positive or negative magnetic field leads to a common  $R = 19.74 \text{ }\Omega$ , yielding a symmetric MR of  $1271 \%$ . The case of  $\Delta x/r_i = 1$  is interesting due to opposite and nonequal behavior in the two directions of magnetic field. For positive fields, we observed  $\text{MR} = 243 \%$ , and in negative fields  $\text{MR} = -76 \%$ , which shows that the device is sensitive to the direction of magnetic field. Studying the current flow of the displaced system ( $\Delta x/r_i = 1$ ) reveals that a small amount of current is flowing around the inclusion at  $B = \pm 1 \text{ T}$ . The current is deflected

toward the grounded contact for  $B = -1$  T, which yields a lower resistance since the current flows almost directly from one contact to the other. For  $B = 1$  T, the current is deflected away from the grounded contact, which in turn forces the current into the metal and upward, causing a longer and more resistive current path. The current flow in the system containing two materials is dissimilar to the single-material systems since  $\mu_{S1} \gg \mu_{S2}$ . The chosen value of  $\mu_{S2} = 2500 \text{ cm}^2/\text{Vs}$  provided the largest effects while keeping a fixed  $\mu_{S1} = 45500 \text{ cm}^2/\text{Vs}$ . At  $B = -1$  T, the majority of the current is deflected around the metal in S1, which changes upon entering S2 as the majority of the current flows directly through the metal. The low mobility causes a weak deflection, thus allowing the current to flow through the metal. This causes the current to focus in a narrow region close to the triple-material boundary. A MR of 456% at  $B = -1$  T is almost double of what the displaced single-material system produced at  $B = 1$  T. However, a positive magnetic field reveals MR = 63% for the two-material device, where the single-material device showed -76%. Combining the two-material device with a left-displaced metal disk yields  $\text{MR}(-1 \text{ T}) = 547\%$  and  $\text{MR}(1 \text{ T}) = -79\%$  (Supplemental Material, Fig. S5 [47]), thus further enhancing the field direction sensitivity compared to the single-material device. The symmetric system yields the largest MR values but the displaced device exhibits other interesting features such as geometry-induced negative MR in a device consisting entirely of nonmagnetic components. Negative MR is often viewed as a product of magnetic materials [51,52] or by chiral anomalies in Weyl metals [53,54], but in this case it arises through an interplay with a Hall signal through the Lorentz force. Breunig *et al.* [52] reports a large negative MR of 98% in a magnetic field of 14 T and  $T = 10$  K, which they claim to be unprecedented in a nonmagnetic system. We report a negative MR of 79% at 1 T and room temperature, which could likely be greatly improved with an optimal geometry.

## VI. PERSPECTIVE

The inclusion of asymmetric elements in magnetoresistive devices have shed light on several important implications:

(1) Weak-field sensitivity: The weak-field sensitivity can be enhanced by embracing asymmetry. We illustrate this point by displacing the metallic inclusion, leading to an enhanced weak-field sensitivity for  $B \rightarrow 0$  which is otherwise a limitation in symmetric devices. Combining the displacement with regions of varying electron mobility resulted in a further enhancement of the weak-field sensitivity. We find that the weak-field sensitivity of asymmetric devices can even be improved beyond what is possible in highly symmetric devices with any bias magnetic field applied to tune them into the most sensitive state. From this perspective, asymmetric device

configurations are highlighted here as a vital tool in device design and a key ingredient to boost weak-field sensitivity.

(2) Large negative magnetoresistance A large negative MR can be induced in nonmagnetic devices using only geometric variations and an interplay with the Hall effect. Albeit, our results are conducted at room temperature using nonoptimal geometries, we obtain an effective negative MR of 79% (see Supplemental Material, Fig. S5), consistent in magnitude to previous nonmagnetic systems exhibiting large negative MR [52]. Further optimization of materials and asymmetric topologies are expected to be key to achieve much higher negative MRs.

(3) On-demand sensor performance: We observe that inducing asymmetry can lead to miscellaneous sensor characteristics, including sensors with step-function responses similar to Fig. 2(b), linearity at  $B = 0$  as shown in Fig. 4(b), or diodelike behavior as shown in Fig. 4(f). Such sensor characteristics are important for, e.g., magnetic switches and weak-field magnetometers. Similar effects of asymmetry are also expected when changing the outer device boundary to a conventional van der Pauw square or Hall bar. Through asymmetric material modification on the nanoscale, one may also produce materials exhibiting nonsaturating, linear positive MR responses present in several recently found materials [55–57], but also devices and materials designed with other characteristics.

(4) Contact permutation: An asymmetric device can be used for multiple purposes by simply changing the current leads. Horizontal displacement of the metallic inclusion can lead to enhanced weak-field sensitivity while vertical displacement retains the high MR of the symmetric system. The symmetry of those systems can either be broken or restored in a single device by permutating the current and voltage contacts. It is therefore possible to switch between several sensor states by contact permutations, in this case a highly magnetoresistive state as shown in Figs. 2(d)–2(f) and a weak-field sensitive state as shown in Figs. 2(a)–2(c) in the same device.

This paper identifies the asymmetric geometric contribution as a key ingredient to achieve superior performance in magnetoresistive devices, which can unlock the potential for designing on-demand sensor responses and unparalleled weak-field sensitivities suitable for detecting biomagnetism and magnetic nanoparticles.

## ACKNOWLEDGMENTS

D.V.C. and N.P. acknowledge funding by Villum Fonden for the NEED project, Grant No. 00027993. D.V.C., N.P., and R.B. acknowledge funding from the Novo Nordisk Foundation Challenge Programme 2021: Smart nanomaterials for applications in life-science, BIOMAG Grant No. NNF21OC0066526.

- 
- [1] E. Grochowski and R. D. Halem, Technological impact of magnetic hard disk drives on storage systems, *IBM Syst. J.* **42**, 338 (2003).  
 [2] M. Holz, O. Kronenwerth, and D. Grundler, Optimization of semiconductor-metal hybrid structures for application in

magnetic-field sensors and read heads, *Appl. Phys. Lett.* **83**, 3344 (2003).

[3] R. H. Kodama, Magnetic nanoparticles, *J. Magn. Magn. Mater.* **200**, 359 (1999).

[4] A. Ito, M. Shinkai, H. Honda, and T. Kobayashi, Medical ap-

- plication of functionalized magnetic nanoparticles, *J. Biosci. Bioeng.* **100**, 1 (2005).
- [5] V. F. Cardoso, A. Francesko, C. Ribeiro, M. Bañobre-López, P. Martins, and S. Lanceros-Mendez, Advances in magnetic nanoparticles for biomedical applications, *Adv. Healthcare Mater.* **7**, 1700845 (2018).
- [6] F. Campos, A. B. Bonhome-Espinosa, R. Carmona, J. D. Durán, P. Kuzhir, M. Alaminos, M. T. López-López, I. A. Rodriguez, and V. Carriel, In vivo time-course biocompatibility assessment of biomagnetic nanoparticles-based biomaterials for tissue engineering applications, *Mater. Sci. Eng. C: Mater. Biol. Appl.* **118**, 111476 (2021).
- [7] G. Binasch, P. Grünberg, F. Saurenbach, and W. Zinn, Enhanced magnetoresistance in layered magnetic structures with antiferromagnetic interlayer exchange, *Phys. Rev. B* **39**, 4828 (1989).
- [8] M. N. Baibich, J. M. Broto, A. Fert, F. Nguyen Van Dau, F. Petroff, P. Etienne, G. Creuzet, A. Friederich, and J. Chazelas, Giant Magnetoresistance of (001) Fe/(001) Cr Magnetic Superlattices, *Phys. Rev. Lett.* **61**, 2472 (1988).
- [9] J. S. Moodera, L. R. Kinder, T. M. Wong, and R. Meservey, Large Magnetoresistance at Room Temperature in Ferromagnetic Thin Film Tunnel Junctions, *Phys. Rev. Lett.* **74**, 3273 (1995).
- [10] T. Miyazaki and N. Tezuka, Giant magnetic tunneling effect in Fe/Al<sub>2</sub>O<sub>3</sub>/Fe junction, *J. Magn. Magn. Mater.* **139**, L231 (1995).
- [11] S. X. Wang and G. Li, Advances in giant magnetoresistance biosensors with magnetic nanoparticle tags: Review and outlook, *IEEE Trans. Magn.* **44**, 1687 (2008).
- [12] D. Su, K. Wu, R. Saha, C. Peng, and J.-P. Wang, Advances in magnetoresistive biosensors, *Micromachines* **11**, 34 (2020).
- [13] S. A. Solin, T. Thio, D. R. Hines, and J. J. Heremans, Enhanced room-temperature geometric magnetoresistance in inhomogeneous narrow-gap semiconductors, *Science* **289**, 1530 (2000).
- [14] T. H. Hewett and F. V. Kusmartsev, Geometrically enhanced extraordinary magnetoresistance in semiconductor-metal hybrids, *Phys. Rev. B* **82**, 212404 (2010).
- [15] J. Moussa, L. R. Ram-Mohan, J. Sullivan, T. Zhou, D. R. Hines, and S. A. Solin, Finite-element modeling of extraordinary magnetoresistance in thin film semiconductors with metallic inclusions, *Phys. Rev. B* **64**, 184410 (2001).
- [16] M. Holz, O. Kronenwerth, and D. Grundler, Magnetoresistance of semiconductor-metal hybrid structures: The effects of material parameters and contact resistance, *Phys. Rev. B* **67**, 195312 (2003).
- [17] J. Sun and J. Kosel, Finite element analysis on the influence of contact resistivity in an extraordinary magnetoresistance magnetic field micro sensor, *J. Supercond. Nov. Magn.* **25**, 2749 (2012).
- [18] T. Hewett and F. Kusmartsev, Extraordinary magnetoresistance: sensing the future, *Open Phys.* **10** (2012).
- [19] T. Zhou, D. R. Hines, and S. A. Solin, Extraordinary magnetoresistance in externally shunted van der Pauw plates, *Appl. Phys. Lett.* **78**, 667 (2001).
- [20] S. Solin, D. Hines, J. Tsai, Y. Pashkin, S. Chung, N. Goel, and M. Santos, Room temperature extraordinary magnetoresistance of nonmagnetic narrow-gap semiconductor/metal composites: application to read-head sensors for ultrahigh-density magnetic recording, *IEEE Trans. Magn.* **38**, 89 (2002).
- [21] S. S. Sosa, Extraordinary magnetoresistance of InSb allows fabrication of a read-head sensor without magnetic noise, *MRS Bull.* **27**, 494 (2002).
- [22] M. Oszwaldowski, S. El-Ahmar, and J. Jankowski, Extraordinary magnetoresistance in planar configuration, *J. Phys. D: Appl. Phys.* **45**, 145002 (2012).
- [23] A. Wittmann, C.-H. Möller, O. Kronenwerth, M. Holz, and D. Grundler, Hybrid ferromagnet/semiconductor nanostructures: Spin-valve effect and extraordinary magnetoresistance, *J. Phys.: Condens. Matter* **16**, S5645 (2004).
- [24] F. S. Terra, A. A. Higazy, G. M. Mahmoud, and A. M. Mansour, (InSb/GaAs)-Au hybrid macro-structure prepared by flash evaporation, *Indian J. Phys.* **84**, 265 (2010).
- [25] D.-C. Wu, Y.-W. Pan, J.-S. Wu, S.-W. Lin, and S.-D. Lin, High-sensitivity two-terminal magnetoresistance devices using InGaAs/AlGaAs two-dimensional channel on GaAs substrate, *Appl. Phys. Lett.* **108**, 172403 (2016).
- [26] J. Wunderlich, T. Jungwirth, V. Novák, A. Irvine, B. Kaestner, A. Shick, C. Foxon, R. Campion, D. Williams, and B. Gallagher, Ordinary and extraordinary Coulomb blockade magnetoresistance in a (Ga, Mn)As single electron transistor, *Solid State Commun.* **144**, 536 (2007).
- [27] J. Lu, H. Zhang, W. Shi, Z. Wang, Y. Zheng, T. Zhang, N. Wang, Z. Tang, and P. Sheng, Graphene magnetoresistance device in van der Pauw geometry, *Nano Lett.* **11**, 2973 (2011).
- [28] S. Pisana, P. M. Braganca, E. E. Marinero, and B. A. Gurney, Graphene magnetic field sensors, *IEEE Trans. Magn.* **46**, 1910 (2010).
- [29] A. L. Friedman, J. T. Robinson, F. K. Perkins, and P. M. Campbell, Extraordinary magnetoresistance in shunted chemical vapor deposition grown graphene devices, *Appl. Phys. Lett.* **99**, 022108 (2011).
- [30] Z. Moktadir and H. Mizuta, Magnetoresistance in inhomogeneous graphene/metal hybrids, *J. Appl. Phys.* **113**, 083907 (2013).
- [31] B. Zhou, K. Watanabe, T. Taniguchi, and E. A. Henriksen, Extraordinary magnetoresistance in encapsulated monolayer graphene devices, *Appl. Phys. Lett.* **116**, 053102 (2020).
- [32] T. Huang, L. Ye, K. Song, and F. Deng, Planar structure optimization of extraordinary magnetoresistance in semiconductor-metal hybrids, *J. Supercond. Novel Magn.* **27**, 2059 (2014).
- [33] L. M. Pugsley, L. R. Ram-Mohan, and S. A. Solin, Extraordinary magnetoresistance in two and three dimensions: Geometrical optimization, *J. Appl. Phys.* **113**, 064505 (2013).
- [34] S. El-Ahmar, W. Koczorowski, A. Poźniak, P. Kuświk, M. Przychodnia, J. Dembowiak, and W. Strupiński, Planar configuration of extraordinary magnetoresistance for 2D-material-based magnetic field sensors, *Sens. Actuators: A Physical* **296**, 249 (2019).
- [35] Y. Shao, S. A. Solin, L. R. Ram-Mohan, and K.-H. Yoo, Optimizing the physical contribution to the sensitivity and signal to noise ratio of extraordinary magnetoresistance quantum well structures, *J. Appl. Phys.* **101**, 123704 (2007).
- [36] C. Rong, H. Zhang, J. Sun, and B. Shen, Geometry and material optimization of the extraordinary magnetoresistance in the semiconductor-metal hybrid structure, *J. Magn. Magn. Mater.* **301**, 407 (2006).
- [37] M. Holz, O. Kronenwerth, and D. Grundler, Optimization of the extraordinary magnetoresistance in semiconductor-metal hybrid



- structures for magnetic-field sensor applications, *Phys. E* **21**, 897 (2004).
- [38] J. Sun, C. P. Gooneratne, and J. Kosel, Design study of a bar-t EMR device, *IEEE Sens. J.* **12**, 1356 (2012).
- [39] J. Sun, Y.-A. Soh, and J. Kosel, Geometric factors in the magnetoresistance of n-doped InAs epilayers, *J. Appl. Phys.* **114**, 203908 (2013).
- [40] H. Tiantian and Y. Lingyun, Simulation optimization of performance for extraordinary magnetoresistance sensor in low-field, in *2013 IEEE 11th International Conference on Electronic Measurement & Instruments* (IEEE, Harbin, China, 2013), pp. 636–640.
- [41] T. H. Hewett and F. V. Kusmartsev, Extraordinary magnetoresistance in hybrid semiconductor-metal systems, *Int. J. Mod. Phys. B* **23**, 4158 (2009).
- [42] J. Sun and J. Kosel, Hall effect enhanced low-field sensitivity in a three-contact extraordinary magnetoresistance sensor, *Appl. Phys. Lett.* **100**, 232407 (2012).
- [43] J. Moussa, L. R. Ram-Mohan, A. C. H. Rowe, and S. A. Solin, Response of an extraordinary magnetoresistance read head to a magnetic bit, *J. Appl. Phys.* **94**, 1110 (2003).
- [44] M. Holz, O. Kronenwerth, and D. Grundler, Enhanced sensitivity due to current redistribution in the Hall effect of semiconductor-metal hybrid structures, *Appl. Phys. Lett.* **86**, 072513 (2005).
- [45] T. D. Boone, N. Smith, L. Folks, J. A. Katine, E. E. Marinero, and B. A. Gurney, Mesoscopic EMR device magnetic sensitivity in I-V-I-V configuration, *IEEE Electron Device Lett.* **30**, 117 (2009).
- [46] T. Zhou, S. Solin, and D. Hines, Extraordinary magnetoresistance of a semiconductor-metal composite van der Pauw disk, *J. Magn. Magn. Mater.* **226-230**, 1976 (2001).
- [47] See Supplemental Material at <http://link.aps.org/supplemental/10.1103/PhysRevB.106.014408> for details.
- [48] T. D. Boone, L. Folks, J. A. Katine, S. Maat, E. Marinero, S. Nicoletti, M. Field, G. J. Sullivan, A. Ikhlassi, B. Brar, and B. A. Gurney, Temperature dependence of magnetotransport in extraordinary magnetoresistance devices, *IEEE Trans. Magn.* **42**, 3270 (2006).
- [49] S. A. Solin, D. R. Hines, A. C. H. Rowe, J. S. Tsai, Y. A. Pashkin, S. J. Chung, N. Goel, and M. B. Santos, Nonmagnetic semiconductors as read-head sensors for ultra-high-density magnetic recording, *Appl. Phys. Lett.* **80**, 4012 (2002).
- [50] J. Sun, S. B. Patil, Y.-A. Soh, and J. Kosel, Strong temperature dependence of extraordinary magnetoresistance correlated to mobility in a two-contact device, *Appl. Phys. Express* **5**, 033002 (2012).
- [51] R. von Helmolt, J. Wecker, B. Holzapfel, L. Schultz, and K. Samwer, Giant Negative Magnetoresistance in Perovskitelike  $\text{La}_{2/3}\text{Ba}_{1/3}\text{MnO}_x$  Ferromagnetic Films, *Phys. Rev. Lett.* **71**, 2331 (1993).
- [52] O. Breunig, Z. Wang, A. Taskin, J. Lux, A. Rosch, and Y. Ando, Gigantic negative magnetoresistance in the bulk of a disordered topological insulator, *Nat. Commun.* **8**, 15545 (2017).
- [53] D. T. Son and B. Z. Spivak, Chiral anomaly and classical negative magnetoresistance of Weyl metals, *Phys. Rev. B* **88**, 104412 (2013).
- [54] X. Huang, L. Zhao, Y. Long, P. Wang, D. Chen, Z. Yang, H. Liang, M. Xue, H. Weng, Z. Fang, X. Dai, and G. Chen, Observation of the chiral-anomaly-induced negative magnetoresistance in 3D Weyl semimetal TaAs, *Phys. Rev. X* **5**, 031023 (2015).
- [55] M. N. Ali, J. Xiong, S. Flynn, J. Tao, Q. D. Gibson, L. M. Schoop, T. Liang, N. Haldolaarachchige, M. Hirschberger, N. P. Ong, *et al.*, Large, non-saturating magnetoresistance in  $\text{WTe}_2$ , *Nature (London)* **514**, 205 (2014).
- [56] C. Chuang, C.-T. Liang, G.-H. Kim, R. Elmquist, Y. Yang, Y. Hsieh, D. K. Patel, K. Watanabe, T. Taniguchi, and N. Aoki, Large, non-saturating magnetoresistance in single layer chemical vapor deposition graphene with an h-BN capping layer, *Carbon* **136**, 211 (2018).
- [57] B. Wu, V. Barrena, F. Mompeán, M. García-Hernández, H. Suderow, and I. Guillamón, Linear nonsaturating magnetoresistance in the Nowotny chimney ladder compound  $\text{Ru}_2\text{Sn}_3$ , *Phys. Rev. B* **101**, 205123 (2020).